AM274 Final Project: Continuous Galerkin Navier-Stokes in 2D

Dylan Nelson, Ariana Minot, Philip Mocz, Pengfei Liu

May 10, 2012

Abstract

We describe the implementation of the continuous Galerkin (CG) method to solve the Navier-Stokes equations on a finite element mesh. We demonstrate the success of the method by solving several 2D model problems, including the backward-facing step, flow past cylinder, and the bifurcated pipe problem. We also post-process simulated flows to study pressure and viscous forces.

1 Introduction

The Navier-Stokes equations are a set of partial differential equations describing the flow of a viscous, incompressible fluid. They represent one of the most physically motivated models in the field of computational fluid dynamics (CFD) and are widely used to model both liquids and gases in various regimes. Use is widespread in such research fields as astrophysics and geophysics as well as in industries including aeronautical, biomedical, chemical, and mechanical. The Navier-Stokes equations are developed in several commercial software packages which are then used to design mechanical machines such as airplanes, boats, bicycles, and cars. In this context the model has been shown to reproduce accurate models of real world fluid problems of practical importance.

Solutions to the Navier-Stokes equations are in general difficult to obtain. Exact analytical solutions exist typically only for problems where the non-linear terms vanish, such as Poiseuille and Couette flow. Mathematical theory of general solutions to N-S in 3D is an open problem and one of the Clay Millennium Prize Problems.

In general, solutions to the time-dependent equations are computed using numerical methods designed to be both highly accurate and highly efficient. We discuss in this paper the implementation of a Navier-Stokes solver using a continuous Galerkin (CG) method for the time-dependent, incompressible fluid flow problem in 2D. We focus on numerical correctness and clarity of algorithmic implementation over any speed considerations. In § 2 we review the mathematical model, while § 3 discusses the numerical implementation. In § 4 we present results on several test problems – the backward-facing step, flow past a cylinder, and bifurcated pipe problem – at various Reynolds numbers and verify the correctness of the code.

2 Mathematical Background

The dimensionless *steady-state* Navier-Stokes equations are:

$$\mathrm{Re}\, \vec{u} \cdot \vec{\nabla}\vec{u} + \vec{\nabla}p = \Delta \vec{u} \tag{1}$$

$$\vec{\nabla} \cdot \vec{u} = 0 \tag{2}$$

where the relations to dimensionful units are:

$$u = u_{\text{units}}/U_0 \tag{3}$$

$$x = x_{\text{units}}/L_0 \tag{4}$$

$$p = p_{\text{units}}/P_0 \tag{5}$$

$$P_0 \equiv \mu U_0/L_0 \tag{6}$$

$$\text{Re} \equiv \rho U_0 L_0/\mu \tag{7}$$

where μ is the dynamic viscosity. Note that if $\text{Re} = 0$ then we have simple Stokes flow. $\text{Re} > 0$ makes the above equations non-linear.

The dimensionless *time-dependent* Navier-Stokes equations are:

$$\frac{\partial \vec{u}}{\partial t} + \text{Re}\,\vec{u} \cdot \vec{\nabla}\vec{u} + \vec{\nabla}p = \Delta\vec{u} \tag{8}$$

$$\vec{\nabla} \cdot \vec{u} = 0 \tag{9}$$

We do not experiment with any additional body forces which could be included as a source term. As before, the relations to dimensionful units are:

$$t = t_{\text{units}}/[\text{Re}L_0/U_0] \tag{10}$$

$$u = u_{\text{units}}/U_0 \tag{11}$$

$$x = x_{\text{units}}/L_0 \tag{12}$$

$$p = p_{\text{units}}/P_0 \tag{13}$$

$$P_0 \equiv \mu U_0/L_0 \tag{14}$$

$$\text{Re} \equiv \rho U_0 L_0/\mu \tag{15}$$

3 Numerical Method

Our numerical technique for solving the Navier-Stokes equations is based on the finite element method, where we search for the solutions of the velocity and pressure fields over an arbitrary computational domain. All code was written in MATLAB. The approach is described below.

3.1 Steady-State Incompressible Navier-Stokes Flow

The steady-state Navier Stokes equations given in (1-2) have a weak-formulation form:

$$\int_\Omega \vec{\nabla}\vec{u} : \vec{\nabla}\vec{w}\,dx + \text{Re}\int_\Omega (\vec{u} \cdot \vec{\nabla}\vec{u}) \cdot \vec{w}\,dx - \int_\Omega p\vec{\nabla} \cdot \vec{w}\,dx = \int_{\partial\Omega_N} (g_{N,1}, g_{N,2}) \cdot \vec{w}\,ds \tag{16}$$

$$\int_\Omega q\vec{\nabla} \cdot \vec{u} = 0 \tag{17}$$

where the Neumann boundary conditions on $\partial\Omega_N$ are given by $(g_{N,1}, g_{N,2})$, and the weak formulation must also satisfy the Dirichlet boundary conditions: $\vec{u}|_{\partial\Omega_D} = (g_{D,1}, g_{D,2})$. The

test functions are $\vec{w} \in V_0 \times V_0$ and $q \in \Pi$. We can set $\vec{w} = (w_1, 0)$, $\vec{w} = (0, w_2)$ to obtain a set of scalar equations.

The above has the following simplified weak formulation: we seek $u_h, v_h \in V_h$ and $p_h \in \Pi_h$ such that $\vec{u}_h|_{\partial\Omega_D} = (u_D, v_D)$ and

$$\int_\Omega \vec{\nabla} u_h \cdot \vec{\nabla} w_{1,h} \, dx + \mathrm{Re} \int_\Omega (u_h \frac{\partial u_h}{\partial x_1} + v_h \frac{\partial u_h}{\partial x_2}) w_{1,h} \, dx - \int_\Omega p_h \frac{\partial w_{1,h}}{\partial x_1} \, dx - \int_{\partial\Omega_N} g_{N,1} w_{1,h} \, ds = 0 \tag{18}$$

$$\int_\Omega \vec{\nabla} v_h \cdot \vec{\nabla} w_{2,h} \, dx + \mathrm{Re} \int_\Omega (u_h \frac{\partial v_h}{\partial x_1} + v_h \frac{\partial v_h}{\partial x_2}) w_{2,h} \, dx - \int_\Omega p_h \frac{\partial w_{2,h}}{\partial x_2} \, dx - \int_{\partial\Omega_N} g_{N,2} w_{2,h} \, ds = 0 \tag{19}$$

$$\int_\Omega q_h \vec{\nabla} \cdot \vec{u}_h = 0 \tag{20}$$

for all $w_{1,h}, w_{2,h} \in V_h$, $q_h \in \Pi_h$.

The discretization is:

$$u_h = \sum_{j=1}^{\mathcal{N}_{\mathrm{vel}}} U_j \phi_j \tag{21}$$

$$v_h = \sum_{j=1}^{\mathcal{N}_{\mathrm{vel}}} V_j \phi_j \tag{22}$$

$$p_h = \sum_{j=1}^{\mathcal{N}_{\mathrm{pres}}} P_j \psi_j \tag{23}$$

where $U \in \mathbb{R}^{\mathcal{N}_{\mathrm{vel}}}$, $V \in \mathbb{R}^{\mathcal{N}_{\mathrm{vel}}}$, $P \in \mathbb{R}^{\mathcal{N}_{\mathrm{pres}}}$ are the coefficient vectors we want to solve for.

The test functions are set to:

$$w_{1,h} = \phi_i, i = 1, \ldots, \mathcal{N}_{\mathrm{vel}} \tag{24}$$
$$w_{2,h} = \phi_i, i = 1, \ldots, \mathcal{N}_{\mathrm{vel}} \tag{25}$$
$$q_h = \psi_i, i = 1, \ldots, \mathcal{N}_{\mathrm{pres}} \tag{26}$$
$$\tag{27}$$

This finite element discretization gives us a nonlinear system of algebraic equations:

$$F_{\mathrm{NS}}(U, V, P) = 0 \tag{28}$$

where $F_{\mathrm{NS}} : \mathbb{R}^{2\mathcal{N}_{\mathrm{vel}}+\mathcal{N}_{\mathrm{pres}}} \to \mathbb{R}^{2\mathcal{N}_{\mathrm{vel}}+\mathcal{N}_{\mathrm{pres}}}$.

We solve for $F_{\mathrm{NS}}(U, V, P) = 0$ using Newton's method. We require an initial guess $(U_0, V_0, P_0) \in \mathbb{R}^{2\mathcal{N}_{\mathrm{vel}}+\mathcal{N}_{\mathrm{pres}}}$, which can typically be the solution to the corresponding Stokes problem (Re = 0). Then for each iterative step k find the update vector $\delta_k \in \mathbb{R}^{2\mathcal{N}_{\mathrm{vel}}+\mathcal{N}_{\mathrm{pres}}}$, which satisfies:

$$J_{F_{\mathrm{NS}}}(U_k, V_k, P_k)\delta_k = -F_{\mathrm{NS}}(U_k, V_k, P_k) \tag{29}$$

where $J_{F_{\mathrm{NS}}}(U_k, V_k, P_k) \in \mathbb{R}^{(2\mathcal{N}_{\mathrm{vel}}+\mathcal{N}_{\mathrm{pres}})\times(2\mathcal{N}_{\mathrm{vel}}+\mathcal{N}_{\mathrm{pres}})}$ is the Jacobian of F_{NS}. We give its explicit formulation in Section 3.2.

The solution is updated after each iteration:

$$(U_{k+1}, V_{k+1}, P_{k+1}) \leftarrow (U_k, V_k, P_k) + \delta_k \tag{30}$$

until $\|\delta_k\|$ falls below a designated tolerance.

3.2 Jacobian of the Steady-State Navier-Stokes Flow, $J_{F_{\mathrm{NS}}}$

The Jacobian $J_{F_{\mathrm{NS}}}(U_k, V_k, P_k) \in \mathbb{R}^{(2\mathcal{N}_{\mathrm{vel}}+\mathcal{N}_{\mathrm{pres}}) \times (2\mathcal{N}_{\mathrm{vel}}+\mathcal{N}_{\mathrm{pres}})}$ has the block form:

$$J_{F_{\mathrm{NS}}} = \begin{bmatrix} A_{uu} & A_{uv} & B_{up} \\ A_{vu} & A_{vv} & B_{vp} \\ B_{up}^T & B_{vp}^T & 0 \end{bmatrix} \tag{31}$$

where:

$$[A_{uu}]_{ij} = \int_\Omega \vec{\nabla}\phi_j \cdot \vec{\nabla}\phi_i \, dx + \mathrm{Re} \int_\Omega \left(u_h \frac{\partial \phi_j}{\partial x_1} + \phi_j \frac{\partial u_h}{\partial x_1} + v_h \frac{\partial \phi_j}{\partial x_2} \right) \phi_i \, dx \tag{32}$$

$$[A_{vv}]_{ij} = \int_\Omega \vec{\nabla}\phi_j \cdot \vec{\nabla}\phi_i \, dx + \mathrm{Re} \int_\Omega \left(v_h \frac{\partial \phi_j}{\partial x_2} + \phi_j \frac{\partial v_h}{\partial x_2} + u_h \frac{\partial \phi_j}{\partial x_1} \right) \phi_i \, dx \tag{33}$$

$$[A_{uv}]_{ij} = \mathrm{Re} \int_\Omega \left(\phi_j \frac{\partial u_h}{\partial x_2} \right) \phi_i \, dx \tag{34}$$

$$[A_{vu}]_{ij} = \mathrm{Re} \int_\Omega \left(\phi_j \frac{\partial v_h}{\partial x_1} \right) \phi_i \, dx \tag{35}$$

$$[B_{up}]_{ij} = -\int_\Omega \psi_j \frac{\partial \phi_i}{\partial x_1} \, dx \tag{36}$$

$$[B_{vp}]_{ij} = -\int_\Omega \psi_j \frac{\partial \phi_i}{\partial x_2} \, dx \tag{37}$$

3.3 Time-Dependent Incompressible Navier-Stokes Flow

The time-dependent Navier Stokes equations given in (8-9) have a weak-formulation form:

$$F_{\mathrm{NS,TD}}(U', V', U^n, V^n, P^n) = 0 \tag{38}$$

A simple way to solve this is with a backward-Euler method:

$$F_{\mathrm{NS,TD}}\left(\frac{U^n - U^{n-1}}{\Delta t}, \frac{V^n - V^{n-1}}{\Delta t}, U, V, P \right) = 0 \tag{39}$$

which makes $F_{\mathrm{NS,TD}}$ a map from $\mathbb{R}^{2\mathcal{N}_{\mathrm{vel}}+\mathcal{N}_{\mathrm{pres}}}$ to $\mathbb{R}^{2\mathcal{N}_{\mathrm{vel}}+\mathcal{N}_{\mathrm{pres}}}$ if we apply discretization of U, V, P. The map $F_{\mathrm{NS,TD}}$ is closely related to the steady-state map F_{NS} and just has the additional terms:

$$\frac{1}{\Delta t} \int_\Omega \sum_{j=1}^{\mathcal{N}_{\mathrm{vel}}} (U_j^n - U_j^{n-1}) \phi_j \phi_i \, dx \quad i = 1, \dots \mathcal{N}_{\mathrm{vel}} \tag{40}$$

4

in the first $\mathcal{N}_{\mathrm{vel}}$ entries and

$$\frac{1}{\Delta t} \int_\Omega \sum_{j=1}^{\mathcal{N}_{\mathrm{vel}}} (V_j^n - V_j^{n-1}) \phi_j \phi_i \, dx \quad i = 1, \dots \mathcal{N}_{\mathrm{vel}} \tag{41}$$

in the next $\mathcal{N}_{\mathrm{vel}}$ entries of the output.

The Jacobian $J_{F_{\mathrm{NS,TD}}}$ is also closely related to the steady-state Jacobian $J_{F_{\mathrm{NS}}}$ and just has the additional contribution:

$$\frac{1}{\Delta t} \begin{bmatrix} M & 0 & 0 \\ 0 & M & 0 \\ 0 & 0 & 0 \end{bmatrix} \tag{42}$$

where

$$M_{ij} = \int_\Omega \phi_j \phi_i \, dx \quad i,j = 1, \dots \mathcal{N}_{\mathrm{vel}} \tag{43}$$

The equations can be numerically solved by employing Newton's method at each time step and taking as an initial guess the solution of the previous time step.

The accuracy of the method can be improved easily by using a higher-order backward differentiation formula (BDF). In our implementation, we use a second-order BDF:

$$F_{\mathrm{NS,TD}}\left(\frac{1.5U^n - 2U^{n-1} + 0.5U^{n-2}}{\Delta t}, \frac{V^n - V^{n-1}}{\Delta t}, U, V, P\right) = 0 \tag{44}$$

3.4   Domain and Solution Space

We subdivide the computational domain Ω of interest in $\mathcal{R}^2$ for each model problem using the `distmesh` package. The vertex (node) locations are placed randomly to achieve a typical spatial resolution within the domain specified by a signed distance functions. A Delaunay triangulation is iteratively regularized until each triangle is roughly equilateral. This leads to better numerical performance when compared to an arbitrary triangulation with a wide range of edge lengths. Note that the `distmesh` package only produces 3-nodes per triangular element, and so we post-process the output to add midpoint nodes, since we require a $\mathcal{N}_{\mathrm{vel}} = 2$ basis.

We identify boundaries in our mesh by testing whether the physical location of a node is within a tolerance error of where we expect the boundary to be. We specify inflow boundary conditions by fixing the values of u_h and v_h on the boundary at each time step. We specify no-slip boundary conditions by fixing u_h and v_h to 0. We specify outflow by using $(g_{N,1}, g_{N,2}) = (0,0)$ Neumann boundary conditions.

We discretize the weak formulation of the Navier-Stokes equation in Equation (38) using the classic Taylor-Hood basis family where the pressure is approximated by linear polynomials ($\Pi_h \in P_1$) and the velocity is approximated by quadratic polynomials ($V_h \in P_2$). Both are continuous across element boundaries. This approach satisfies the constraint that the order of basis of the pressure must be less than that of the velocity in order to avoid singular matrices during the solution step.

4 Model Problems

In this section, we apply the numerical methods discussed above to several 2D model problems.

4.1 Backward-Facing Step
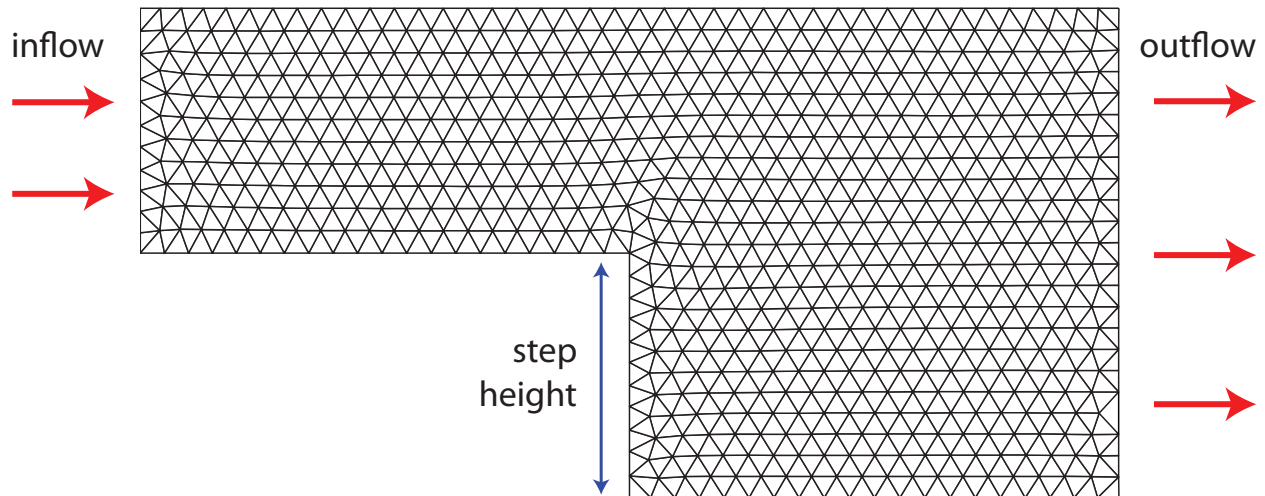
Figure 1: Domain geometry for the backward-facing step problem and a representative low-resolution mesh. The inflow and outflow boundaries on the left and right faces are indicated, while the top and bottom faces have no-slip enforced.

This case examines turbulent fluid flow past a "backward-facing step" at increasing Reynolds number. The geometry of the domain and a representative low-resolution mesh is shown in Figure (1). We take the rectangular domain Ω such that $0 < x < 2$, $0 < y < 1$ with the step vertex at $x = 1$, $y = 0.5$ (a step height of 0.5). We specify a parabolic inflow velocity on the left boundary (peak velocity 1), no-slip on the top and bottom, and outflow on the right. Characteristic solutions of the steady-state at low $\mathrm{Re} = 10$ for both velocity components and the pressure are shown in Figures (2)-(4). The velocity-field is post-processed to visualize streamlines of the flow in Figure (5) where the laminar turbulent boundary past the step can be seen in the circulation region.

The size of the turbulent region increases with higher Reynolds number, as expected. The flow demonstrates the same behavior as in the AM 274 chapter II.5 slides. We consider this qualitative verification of the correctness of our code.
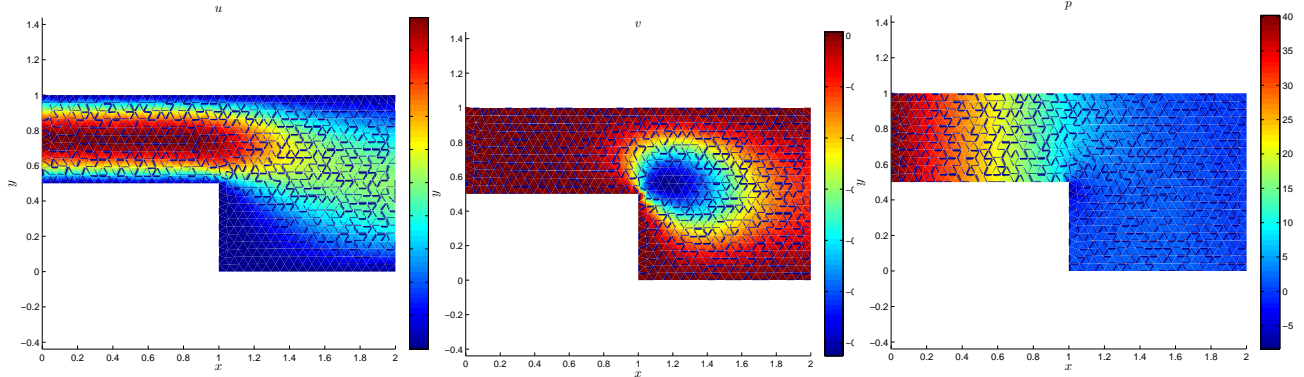
Figure 2: Backward-facing step u solution at Re = 10.

Figure 3: Same as previous, for v solution.

Figure 4: Same as previous, for p solution.
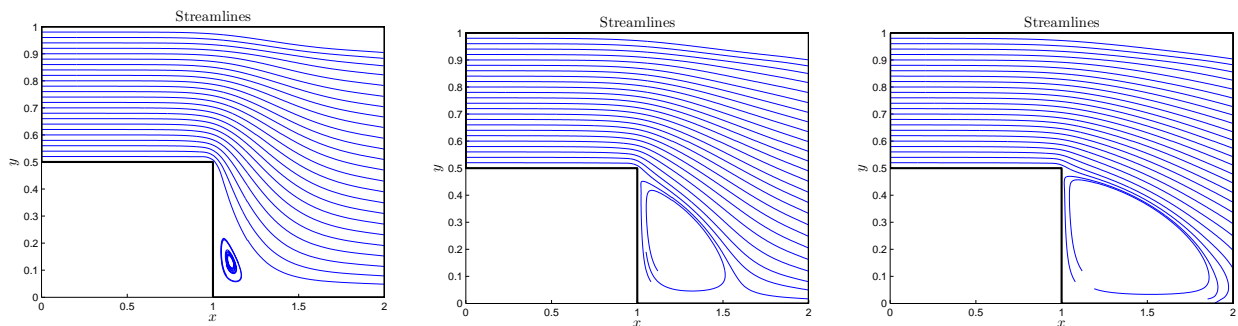
Figure 5: Backward-facing step streamlines for Re = 10.

Figure 6: Same as previous, for Re = 50.

Figure 7: Same as previous, for Re = 100.

4.2 Flow Past a Cylinder

In this test problem, we look at the 2D cross-section flow past a cylinder. We create a mesh as shown in Figure 8. The domain is $[0, 4] \times [0, 2]$ with a circle of radius 0.2 centered at $(1.5, 1)$. The mesh has higher resolution in regions we expect the flow to be more complicated, such as around the cylinder and behind it. The left boundary has parabolic inflow (max velocity 1). No-slip boundary conditions are imposed on the top, bottom, and cylinder. Outflow is imposed on the right boundary.

First, we test the *time-dependent* Navier Stokes solver. We investigate a Reynolds number 40 flow. We use the Stokes solution as the initial condition and show the evolution of the fluid (u is plotted) in Figures 9. The fluid adjusts to a steady wake behind the cylinder on the order of the viscous timescale. The flow is the same as would be obtained by solving the steady-state Navier Stokes equations with Reynolds number 40. Plots of the pressure and velocity in the final state are shown in Figures (10)-(12)

We also investigate the forces on the cylinder due to pressure and viscosity as a function of Reynolds number. Here we consider the forces due to steady state (time-independent) flow. We investigate Reynolds numbers of in the range 0.1–100. The viscous and pressure forces on the cylinder (boundary ∂C) are:

7
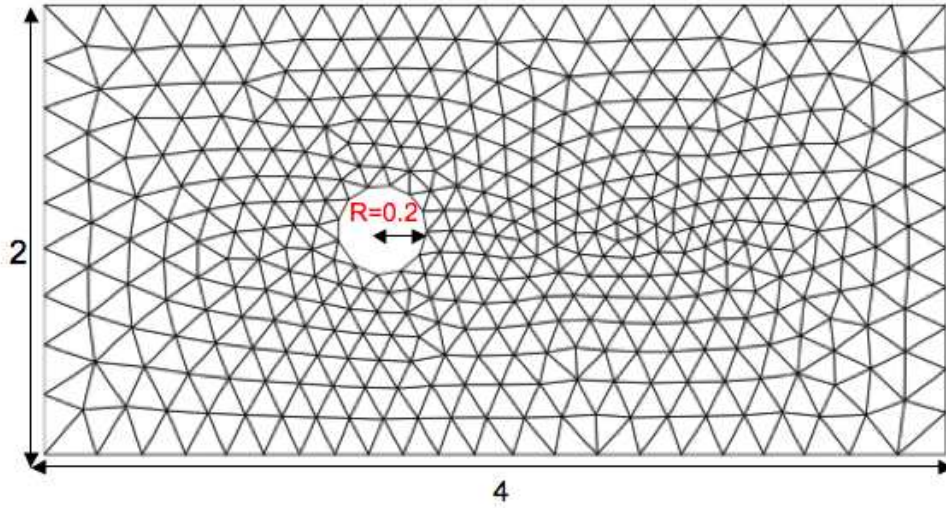
Figure 8: Domain geometry for the flow past a cylinder. There is inflow on the left, outflow on the right, and no-slip on the top, bottom, and cylinder boundaries.
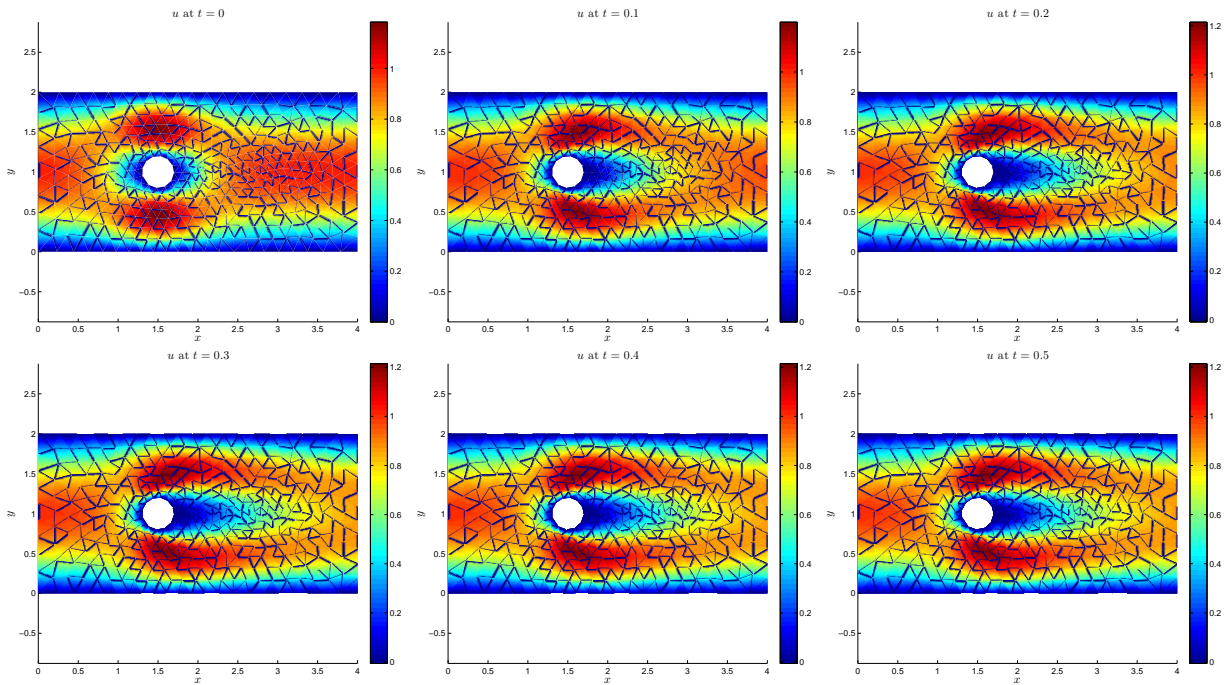
Figure 9: Time evolution of flow past cylinder, Re = 40. Initial condition is Stokes flow. Steady state is reached on order of the viscous timescale. Note the breaking of symmetry in front and behind the cylinder in the flow with non-zero Reynolds number.

$$\vec{F}_{\text{visc}} = -\mu \int_{\partial C} (\vec{\nabla}\vec{u} + (\vec{\nabla}\vec{u})^T)\vec{n}\,ds \tag{45}$$

8
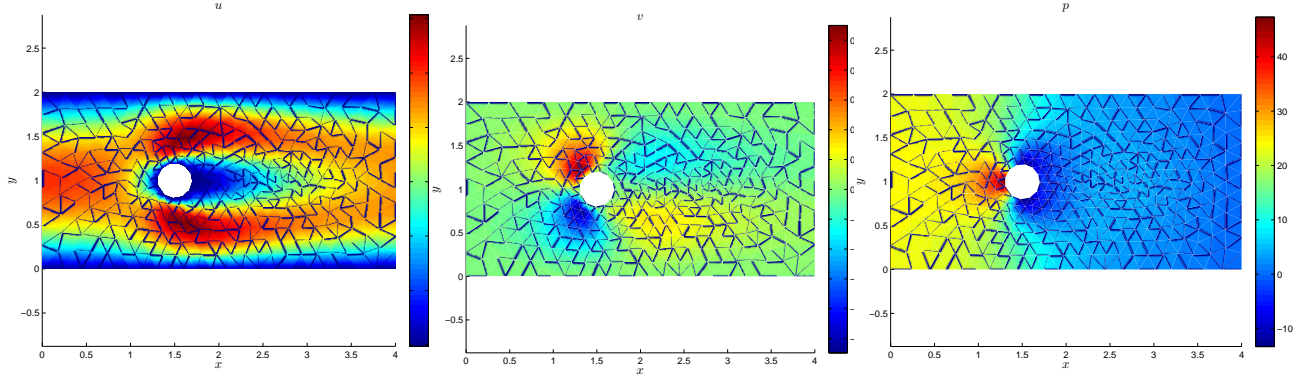
Figure 10: Flow past cylinder, u solution at Re = 40.

Figure 11: Same as previous, for v solution.

Figure 12: Same as previous, for p solution.

$$\vec{F}_{\text{pres}} = \int_{\partial C} p(s)\vec{n}\,ds \qquad (46)$$

where $\vec{n}$ is the outward unit normal to the cylinder.

These forces can be normalized by the dynamic pressure $P_{\text{dynamic}} \sim \frac{1}{2}\rho V_0^2$. This turns out to be equivalent to dividing the unitless $\vec{F}_{\text{visc}}$ and $\vec{F}_{\text{pres}}$ by the global Reynolds number. These normalized values are called drag coefficients, C_D.

The pressure and viscous forces are shown in Figure 13 (compare with Figure 1 of Henderson [1995]). As expected, the pressure force is larger, and both forces decrease with Reynolds number relative to the dynamic pressure. In addition, the drag coefficient $C_D \propto \text{Re}^{-1}$ for Re < 100, shows excellent quantitative agreement with theoretical expectations for a steady wake.

At high Reynolds numbers of Re $\gtrsim$ 100, instabilities are expected which lead to vortex shedding. This will result in the drag coefficient flattening to ~ 1. In general this phenomenon can be captured by solving the time-dependent flow instead on a high resolution grid. We attempted to reproduce this interesting effect with uniform "windtunnel" type flow past both circular and rectangular obstructions but did not immediately see vortex shedding. The relatively slow performance of our time dependent code prevented any more exhaustive exploration of the parameter space within which vortex shedding takes place.

4.3 Bifurcated Pipe

In this test problem, we examine flow in symmetric and asymmetric bifurcated pipes. The geometries of the two domains are shown in Figures (14) and (15). We specify a parabolic inflow velocity on the left boundary (peak velocity 1), outflow on the right boundaries, and no-slip boundary conditions elsewhere. We compare the steady-state solutions at Re = 10 for the symmetric and antisymmetric pipes. Both velocity components and the pressure are plotted in Figures (16)-(21). The outflow boundary conditions enforce that the mean pressure across the outflow boundary is zero, causing the pressure gradient of the shorter pipe branch to be greater [Rannacher,1999]. This results in greater flow going through the shorter pipe branch than through the longer pipe branch. Our results reproduce this expected behavior. The streamlines are shown for the symmetric pipe at Reynolds number

9
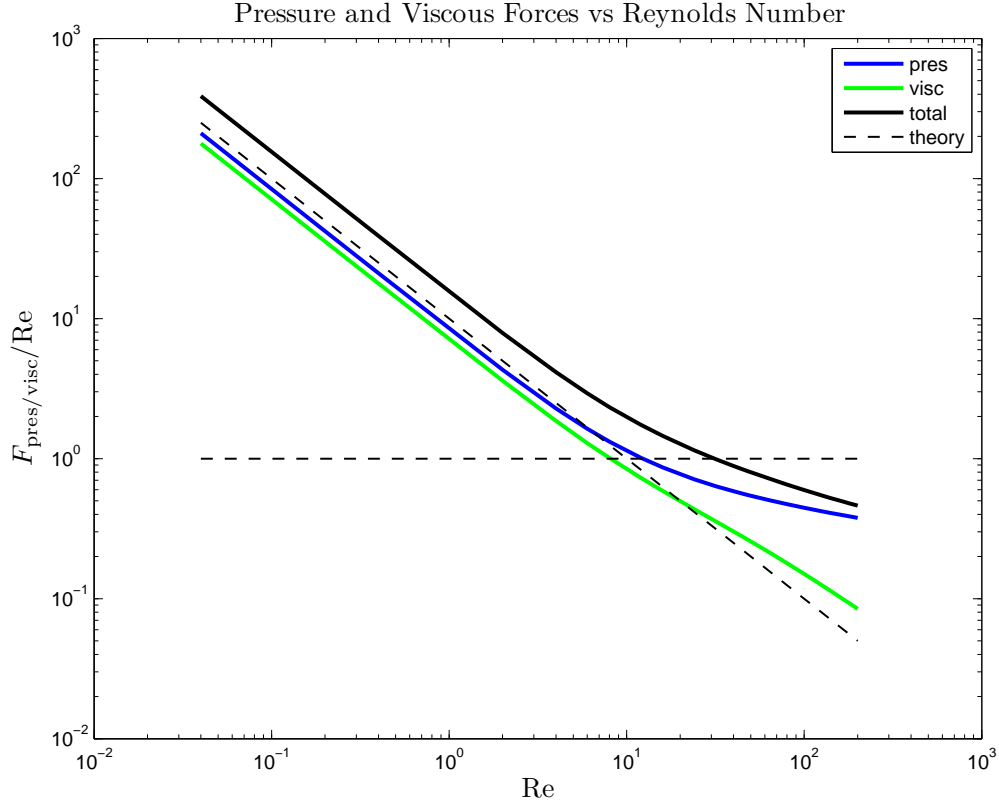
Figure 13: Steady-wake pressure and viscous forces normalized by the dynamic force on the cylinder as a function of Reynolds number. For Reynolds numbers less than ~ 100, these drag coefficients are expected to be inversely proportional to the Reynolds number.

10 and 100 in Figures (22) and (23). The size of the turbulent region again increases with Reynolds number as expected.

5   Concluding Remarks

We have successfully created a CG solver for the Navier-Stokes equations and applied it to several test problems. We deliberately looked at problems that are fairly simple and not too computationally intensive. Our method can easily be extended to 3D, but would require more computational resources. Higher Reynolds number flows require greater mesh resolution due to thin-boundary layers that can form, thus requiring more computational power and memory as well. In addition, a stabilization method such as Streamline Upwind Petrov-Galerkin (SUPG), which introduce extra terms into the weak form to minimize spurious oscillations in convection-dominated flows, may need to be employed for higher Reynolds number flows.
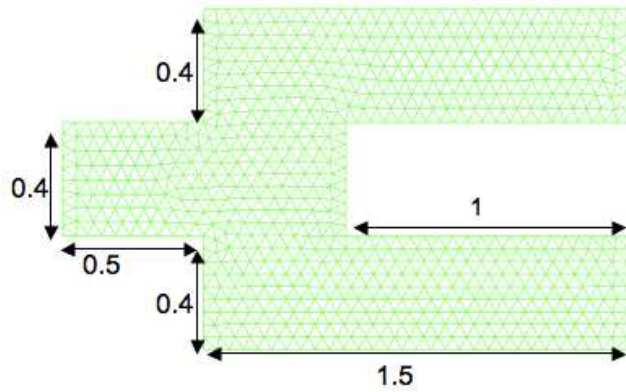
Figure 14: Dimensions of the bifurcated pipe setup.
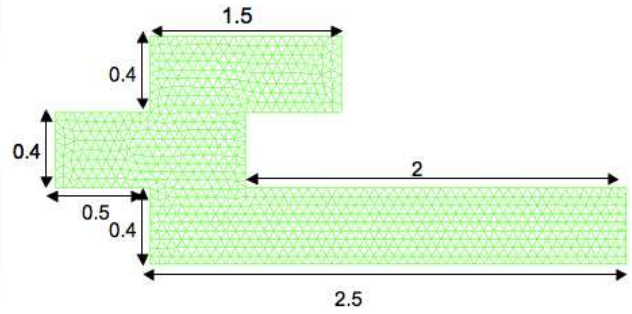
Figure 15: Dimensions of the asymmetric bifurcated pipe setup.
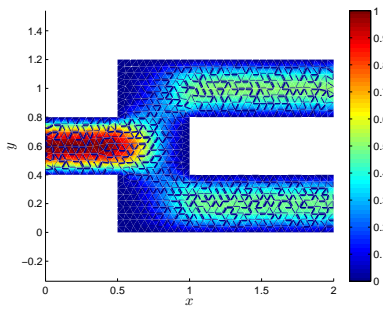
Figure 16: Bifurcated pipe flow u solution at Re = 10.
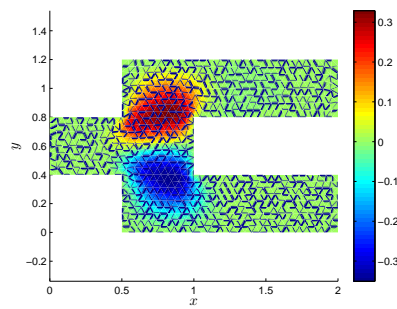
Figure 17: Bifurcated pipe flow v solution at Re = 10.
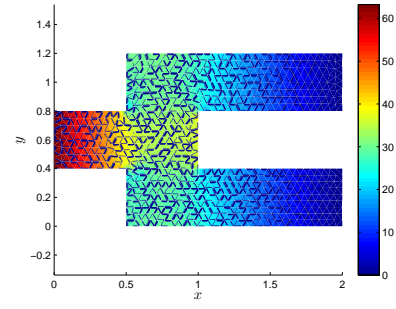
Figure 18: Bifurcated pipe flow p solution at Re = 10.
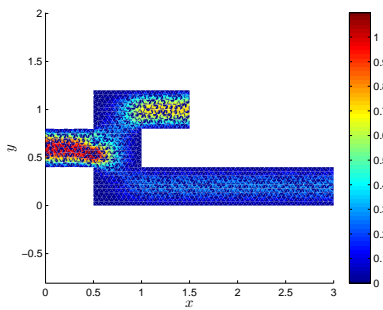
Figure 19: Asymmetric bifurcated pipe flow u solution at Re = 10.
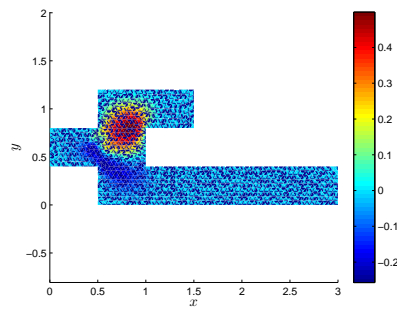
Figure 20: Asymmetric bifurcated pipe flow v solution at Re = 10.
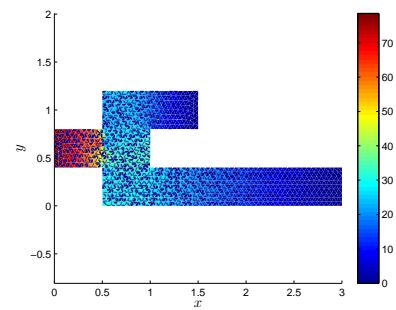
Figure 21: Asymmetric bifurcated pipe flow p solution at Re = 10.

References

R.D. Henderson. Details of the drag curve near the onset of vortex shedding. *Phys. Fluids*, 7:2102–2104, 1995.
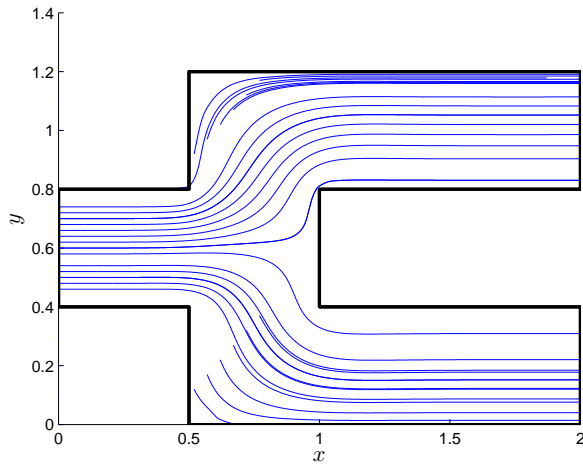
Figure 22: Backward-facing step streamlines for Re = 10.
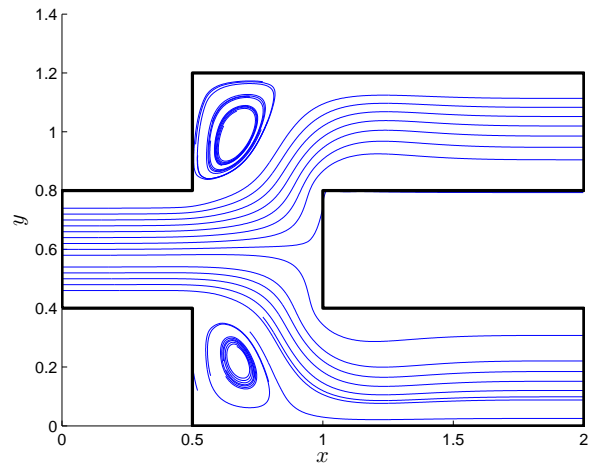
Figure 23: Same as previous, for Re = 100.

Rannacher R. Finite element methods for the incompressible navier-stokes equation, 1999. URL http://numerik.iwr.uni-heidelberg.de/Oberwolfach-Seminar/CFD-Course.pdf.